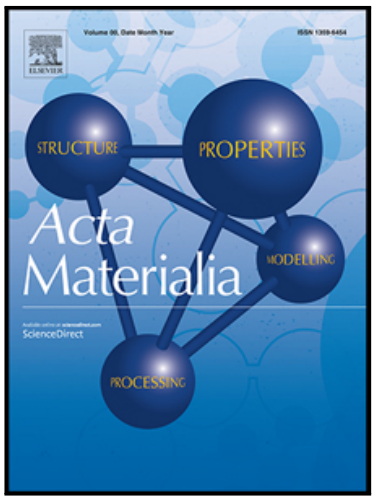

Thermal Stability of Thin Au Films Deposited on Salt Whiskers

Ehud Almog , Vadim Derkach , Amit Sharma ,
Amy Novick-Cohen , Julia R. Greer , Eugen Rabkin

PII: S1359-6454(20)30974-5
DOI: https://doi.org/10.1016/j.actamat.2020.116537
Reference: AM 116537

To appear in: *Acta Materialia*

Received date: 22 July 2020
Revised date: 30 November 2020
Accepted date: 30 November 2020

Please cite this article as: Ehud Almog , Vadim Derkach , Amit Sharma , Amy Novick-Cohen , Julia R. Greer , Eugen Rabkin , Thermal Stability of Thin Au Films Deposited on Salt Whiskers, *Acta Materialia* (2020), doi: https://doi.org/10.1016/j.actamat.2020.116537

Thermal Stability of Thin Au Films Deposited on Salt Whiskers

*Ehud Almog[1], Vadim Derkach[2], Amit Sharma[1,3], Amy Novick-Cohen[2], Julia R. Greer[4] and Eugen Rabkin[1]**

[1]Department of Materials Science and Engineering, Technion – Israel Institute of Technology, 3200003 Haifa, Israel

[2]Department of Mathematics, Technion – Israel Institute of Technology, 3200003 Haifa, Israel

[3]EMPA, Swiss Federal Laboratories for Materials Science and Technology, Laboratory for Mechanics of Materials and Nanostructures, Feuerwerkerstr. 39, Thun CH-3602, Switzerland

[4]Materials Science, California Institute of Technology, Pasadena CA 91125, USA

Keywords: Gold thin films; morphology; theory and modeling; diffusion; solid state dewetting.

ABSTRACT

Thin metal films deposited on patterned or rough substrates play an increasing role in microelectronics, sensing, catalysis, and other areas of nanotechnology. However, the thermal stability and solid state dewetting of thin metal films with complex three-dimensional architecture is still poorly understood. In this work we employed a model system of nanocrystalline Au thin films deposited on prismatic single crystalline KCl whiskers to study the solid state dewetting of thin films in a three-dimensional setting. The arrays of KCl whiskers were grown on porous substrates under well-defined humidity and temperature conditions. Single crystalline prismatic KCl whiskers with a very high aspect ratio, [001] axis and {100} side facets were obtained. The whiskers were coated with thin conformal Au films of 20-30 nm in thickness. The annealing of these core-shell whiskers at the temperature of 350^{o}C resulted in solid state dewetting of the Au film, with the dewetting processes occurring much faster along the whisker edges than on the side facets. The orientation relationships between Au and KCl were determined by employing similarly prepared thin Au films deposited on the flat KCl (100) substrates. Inspired by our experimental results, we developed a numerical model describing the curvature-gradient driven and surface diffusion-controlled growth of a hole in the thin film deposited on a curved substrate. The model predicted the growth of anisotropic elliptical holes elongated along the whisker axis. We discuss the experimental results in terms of the proposed model, indicating the importance of the change in orientation relationship between the Au grains and KCl whisker along the whisker edges.

1. INTRODUCTION

Thermal stability of thin solid films has been extensively studied in recent decades [1–5]. The driving forces for the microstructure and morphology changes in the films include defects annihilation, elastic energy reduction, and minimization of surface and interface energies. Thin films of metals and semiconductors constitute the elementary building block of the integrated circuits in microelectronics. While thin film stability is essential for the reliable functioning of electronic components [6,7], various thin film instabilities have been successfully employed in a bottom-up approach to produce nanoparticles for applications in photonics [8], sensing [9,10], and for the catalytic growth of semiconductor nanowires and carbon nanotubes [11–13].

When thin metal films deposited on ceramic substrates are exposed to an elevated temperature below the melting point of the metal, they can undergo solid-state dewetting (SSD) instability. The process typically begins with the formation of holes in the film that expand and merge with each other, resulting in the formation of isolated metal islands which eventually evolve into single crystalline metal particles exhibiting equilibrium crystal shapes [1]. The thermodynamic driving force for this process is the reduction of the surface and interface energies of the system, while its kinetics is controlled by self-diffusion on the metal surface.

Thin films are also widely employed in design of three dimensional nanostructures exhibiting novel mechanical [14,15], electrical [16] and electrochemical [17] properties. In these complex structures, regions of high surface curvature play an important role in the mechanical behavior and thermal stability. According to Herring [18], the chemical potential of atoms located on these curved surfaces is different from that of the atoms on a flat surface, providing an additional driving force for mass transport in the near-surface region which affects the thermal stability of the film.

Several studies have addressed the problem of SSD on curved substrates. Giermann and Thompson [19] fabricated patterned substrates with a pyramidal topography to guide the formation of particles into pits. Varying the ratio between pit size and initial film thickness resulted in different morphologies, where some specific ratio yielded a single particle per pit. It was proposed that the governing mechanism for this guided SSD is related to the enhanced surface diffusion at the curved pit edge. Klinger and Rabkin [20] proposed a method to simulate the behavior of nanoparticles on a rigid curved substrates. They described how a single nanoparticle on a curved substrate can move by rotation controlled by surface and interface diffusion of particle atoms. Jiang et al. [21] suggested a mathematical model based on a thermodynamic variational approach to simulate the agglomeration of thin films into nanoparticles on the curved surfaces. In their work they examined how the curvature of a substrate affects the pinch-off of large islands and the migration of small particles. In addition, they applied their model to the analysis of the guided SSD experiment of Gierman and Thompson [19]. Although the previous studies covered many aspects of SSD of thin films deposited on curved substrates, only a handful of experimental works analyzed the SSD behavior of thin films deposited on substrates with well-characterized curvature. Moreover, the effect of substrate curvature on hole nucleation during the initial stages of SSD has not been addressed.

The aim of the present work is to understand the SSD behavior of thin films deposited on substrates with complex three-dimensional geometry. To this end, we produced high aspect ratio KCl salt whiskers of several micrometers in cross-sectional size, and coated them with Au thin films to form a core-shell structure. We studied the SSD behavior of these core-shell structures experimentally, and we discuss our observations in terms of a mathematical model and numerical simulations, based on a surface diffusion which is curvature-gradient driven [22,23]. Our model

provides us with a tool for analyzing the SSD behavior of thin films deposited on curved substrates in a wide range of substrate curvatures, metal-substrate contact angles, and hole sizes.

2. Experimental

2.1. Whisker growth

We utilized the technique of Zhang et al. [24,25] for the growth of KCl whiskers, which in turn relies on the previous observations of Gyulai [26] and Shichiri [27]. In this technique, glass slides are cleaned in an ultrasonic bath containing detergent water, then rinsed in ethanol and distilled water, and dried at 120^{o}C for 1 hour. The glass slides are dip coated in an aqueous solution containing 10 wt.% of dispersed silica nanoparticles (Cabot PG022) to form a porous surface. The dip coating is performed in a modified Instron tensile testing device at a constant pulling rate of 0.2 mm/sec. One side of the slides is wiped clean with ethanol leaving only 1 coated surface, and then they are placed for 1 hour at 70^{o}C in an oven for final drying. A custom-made humidity cell comprised of a double chamber glove box was designed to allow optimized conditions for whiskers growth. The humidity in the cell is maintained ~75% RH by a large saturated NaCl reservoir in equilibrium with its vapor, and a small fan on the top of the cell to control the evaporation rate.

We prepared cylindrical 100ml beakers with 40ml 2.9wt% KCl solution comprised of HPLC-grade water (SIGMA-ALDRICH, USA) and KCl salt (Merck KGaA, Germany). The coated slides are tilted 60^{o} inside the beaker, so that only the lower third of the slide is immersed in the solution, with the coated side pointing upwards (Fig. 1). The beakers with the slides are inserted into the humidity cell for a period of 24-72 h. Within the growth period, rectangular whiskers with varying dimensions of 0.05-5mm in height and 0.5-20μm in thickness are formed.

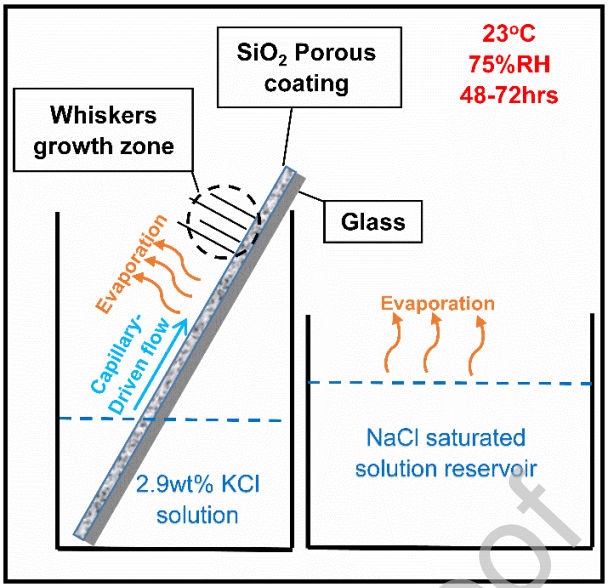

Fig. 1 – An illustration of the experimental setup for whiskers growth(not to scale). A large reservoir of saturated NaCl solution maintains the relative humidity at approximately 75% RH.

2.2.Thin film deposition

The deposition of the Au coating was performed in an e-beam evaporator (Airco Temescal BJD) under high vacuum of ~$3x10^{-7}$ Torr at room temperature with deposition rate of 0.3 nm/sec. The slides with the whiskers were tilted 45° towards the target to obtain homogenous deposition on the whiskers. Because of this tilt, the actual thickness of the Au coating on the whiskers was in the range of 20-30 nm, which is ~30% of the nominal thickness of 100 nm.

2.3.Thermal annealing

The annealing was performed in a Rapid Thermal Annealing (RTA, ULVAC MILA 5000) furnace in the temperature range of 300 – 600 °C for up to 5 hours. For longer annealing (up to

72 h) a resistance tube furnace was used. All thermal treatments were performed in an ambient atmosphere.

2.4. Characterization

All samples were characterized by high resolution scanning electron microscope (HRSEM; Zeiss Ultra Plus) under standard imaging conditions of 4 kV acceleration voltage and 30 μm aperture. Electron back scattered diffraction (EBSD) images were taken on a 70° pre-tilted sample, using a QUANTAX (Bruker) detector and analysis software. Cross section samples were fabricated and examined with the aid of a Focused Ion Beam (FIB; FEI Helios Nanolab G^3 UC) instrument. Electron diffraction patterns were acquired in a Transmission Electron Microscope (TEM; FEI Tecnai G^2 T20) operated at 200 kV, on cross section samples prepared by the lift out method in FIB [28].

X-ray Difraction (XRD; Rigaku SmartLab) measurements were conducted on flat (100) KCl wafers (MTI corporation) coated with a 30 nm thick Au film with the same deposition parameters as those employed in the whisker coating. The samples were aligned by the rocking curve method on the KCl (200) reflection. Cu Kα radiation in parallel beam geometry with a double (220) Ge monochromator were used to obtain high resolution. In-plane pole figure spectra were obtained using steps of 5° and 3° for the azimutal rotation, φ, and the diffraction angle, χ, respectively.

3. Results

3.1. Three dimensional morphology of thin Au film

The three-dimensional architecture of the whiskers' array poses a challenge when uniform coating is necessary. Uniform thickness of the film is important for further analysis of the SSD in the system. For the purpose of uniformity, the substrate with whiskers was tilted by 45^{o} with respect to the deposition target and placed on a rotating stage inside the evaporation chamber. Fig. 2 shows a cross section (CS) FIB micrograph of a uniformly coated whisker, which indicates the continuity of the Au film both on the facets of the whisker and at its edges. Thickness measurements on different whiskers indicated that nominal deposition thickness of 100 nm resulted in Au coating of approximately 20-30 nm in thickness on the whisker sides. This difference between the nominal and measured thicknesses is a result of the rotating stage tilt, which enables facet coating only opposite to the evaporator Au target. The radius of curvature at the edges was measured for several whiskers and found to vary significantly from hundreds of nanometers to 1-2 μm. Electron diffraction pattern produced in the TEM indicated that the whisker growth direction and side facets are [001] and {100} respectively, reflecting the cubic symmetry of KCl rocksalt structure. High resolution TEM images could not be obtained because of fast evaporation of KCl under the energetic electron beam.

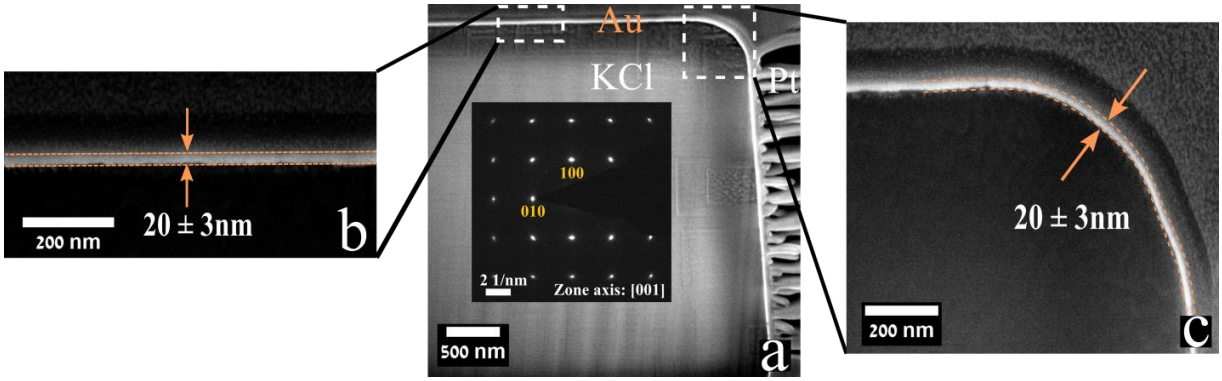

Fig. 2 – (a) Cross section FIB micrograph of the KCl whisker coated with a 20 nm - thick layer of Au. The measurements of the Au film thickness and its homogeneity and conformity were performed on the (b) upper side of the cross section coinciding with the ion beam focal plane. The Au film thickness is roughly 20nm on the (b) upper facet and (c) upper right edge, and the radius of curvature at the edge is r=1.4μm.

3.2. The texture of the Au coating and its orientation relationship with the KCl whisker

Gold films deposited on a rocksalt single crystals can display different orientation relationships (ORs), depending on the temperature and chemical purity of the salt surface. Several studies have shown that heteroepitaxial growth of $(100)_{Au} \parallel (100)_{KCl}$ is possible on clean cleaved salt surfaces under ultra-high vacuum, elevated temperatures and slow deposition rates [29–32]. In the case of KCl whiskers produced in the present work, the preparation method results in exposure of the surface of the crystals to the ambient, and cleavage is impossible because of the small dimensions of the whiskers. We determined the orientation relationship and texture of the 30 nm-thick Au films deposited on the (200) oriented reference KCl wafers under deposition conditions identical to those employed in producing the KCl-Au core-shell whiskers. In Fig. 3 a general θ-2θ scan of the as-deposited film shows a typical [111] out of plane orientation of the

Au grains. This fiber texture remains unchanged after thermal annealing at 350^{o}C for 5 h, as determined both by XRD and HRSEM. The observed XRD peaks exhibit narrowing after annealing because of defect annihilation and increase of the coherence length in the sample. Pole figures of both the as-deposited and annealed (5 h at 350 ^{o}C) films (Fig. 3a, b) showed general random in-plane orientations of the Au grains. However, careful examination of the {111} ring of the annealed film revealed weak oscillations with a period of 30^{o} along the ϕ direction, as seen in Fig. 3c. Similar oscillations were observed in thin Au films deposited on the basal plane-oriented sapphire substrate [33]. They were related to the local minima of the film-substrate interface energy corresponding to the good matching between Au and sapphire lattices. However, these oscillations are somewhat surprising in the present context because of the four-fold symmetry of the {100} KCl substrate.

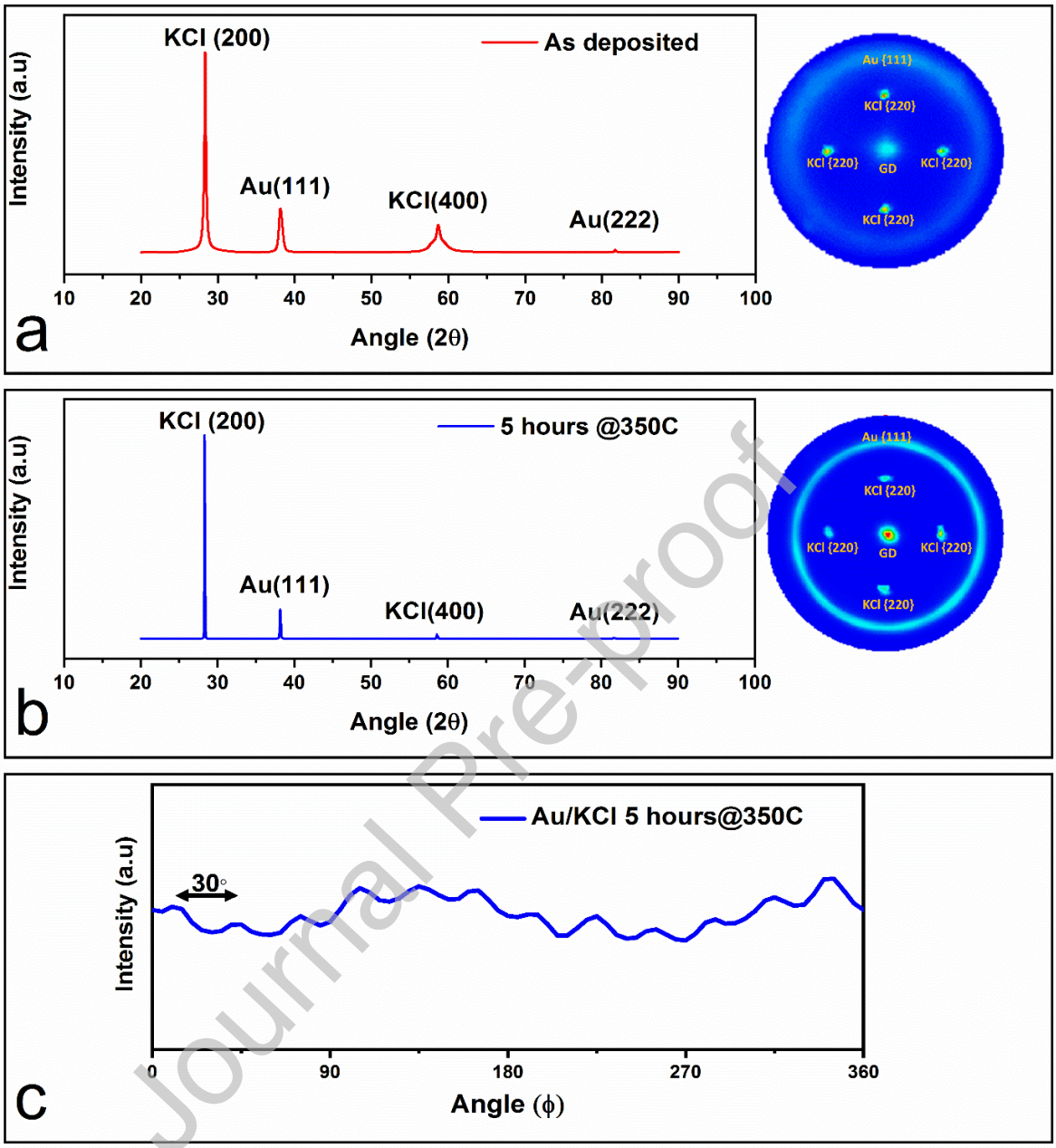

Fig. 3 – XRD θ-2θ and in-plane pole figure patterns of (a) an as deposited 30 nm-thick Au film on KCl (2 0 0) substrate and (b) the same film after annealing at 350°C for 5 h. The out of plane OR remains the same, while the diffraction peaks are narrowed after annealing. The ϕ scan of the (111) diffraction ring of the annealed film exhibits an oscillation wavelength of 30°(c).

The EBSD maps of the Au film on the KCl substrate after annealing for 1 h at 350 ^{o}C verified two sets of twin OR variants color-coded red and green in Fig. 4. Variants 1 and 3 correspond to a $[1\bar{1}0]_{Au} \| [010]_{KCl}$ and $[\bar{1}\bar{1}2]_{Au} \| [001]_{KCl}$ in-plane orientation relationships, respectively, each exhibiting 3 fold symmetry around the [111] normal. Variants 2 and 4 are obtained by rotation of 60^{o} around the [111] normal from the variants 1 and 3, respectively, which means that the variants within each of the two couples (1-2 and 3-4) are in the twinning orientation relationship with each other. The inverse pole figure (IPF) map in Fig. 4 is produced with respect to the [111] direction as in the XRD pole figure map. The EBSD technique allows coloring of the grains in accordance with their in-plane orientation as specified in the IPF color legend. Specifically, the grains are colored in the micrograph according to their in-plane orientation which points to the right side of the image (i.e. *x*-axis of the IPF). The two couples of the OR variants are equivalent with respect to the nearest-neighbor configurations of the Au and KCl atoms on either side of the interface, with possible differences with respect to the second-nearest and higher-order neighbors. Thus, these four ORs are consistent with the 30^{o} oscillations along the ϕ direction in the pole figure of Fig. 3. Most likely, they correspond to the local cusps in the dependence of the Au-KCl interface energy on the in-plane orientation of the Au grains. The micrograph also shows clearly that the grain size in the annealed film corresponds roughly to the film thickness (30 nm).

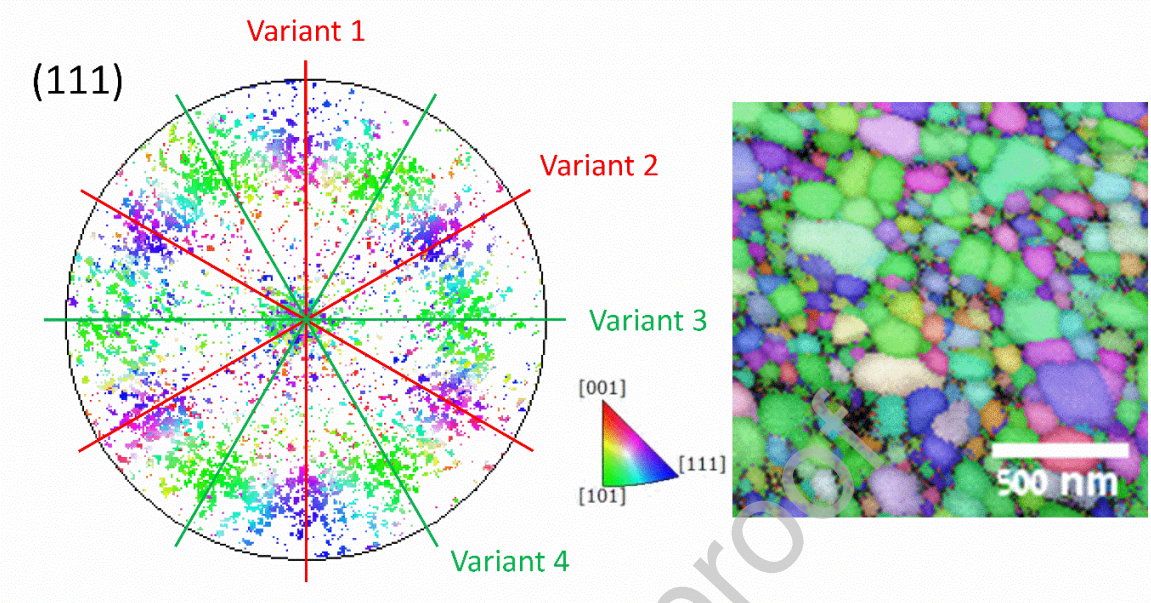

Fig. 4 – Inverse pole figure (IPF) map produced by EBSD imaging of the Au film on a KCl substrate after annealing for 1 h at 350 °C. The color coding corresponds to the in-plane orientation of the grains. Two sets of OR variants marked in green and red correspond to $[1\bar{1}0]_{Au} \parallel [010]_{KCl}$ *and* $[\bar{1}\bar{1}2]_{Au} \parallel [001]_{KCl}$ *ORs, respectively.*

3.3. Thermal stability of gold film on whiskers' edges

The unique geometry of the KCl rocksalt whiskers enables investigation of the thermal stability of the Au film on both flat facets and on the curved edges. The Au-coated whiskers were annealed at the temperature of 350 ^{o}C for different times to observe the various stages of the dewetting process. Fig. 5 shows the gold film evolution after different annealing times, beginning with the formation of holes (2, 3 and 10 min), followed by the formation of islands (60 min) and finally particles (7 days). The distribution of holes in the whisker annealed for 2 min is homogeneous, without any preference for the edges. The formed holes are round, uniform in size, and have a diameter of approximately 30 nm. After annealing different samples for 3 and 10 minutes, the whisker edges are visibly more exposed than its flat side facets. The Au film becomes fully agglomerated into well separated islands after annealing for 60 min, with the islands on the edge being significantly smaller than their counterparts on the flat facets. Fully equilibrated Wulff shaped Au particles are not formed even after very long annealing for 7 days, because of the low homologous annealing temperature ($0.47T_m$, where T_m is the melting temperature of Au), and the defect-deficient nature of the single crystalline Au particles which impedes their equilibration [34,35].

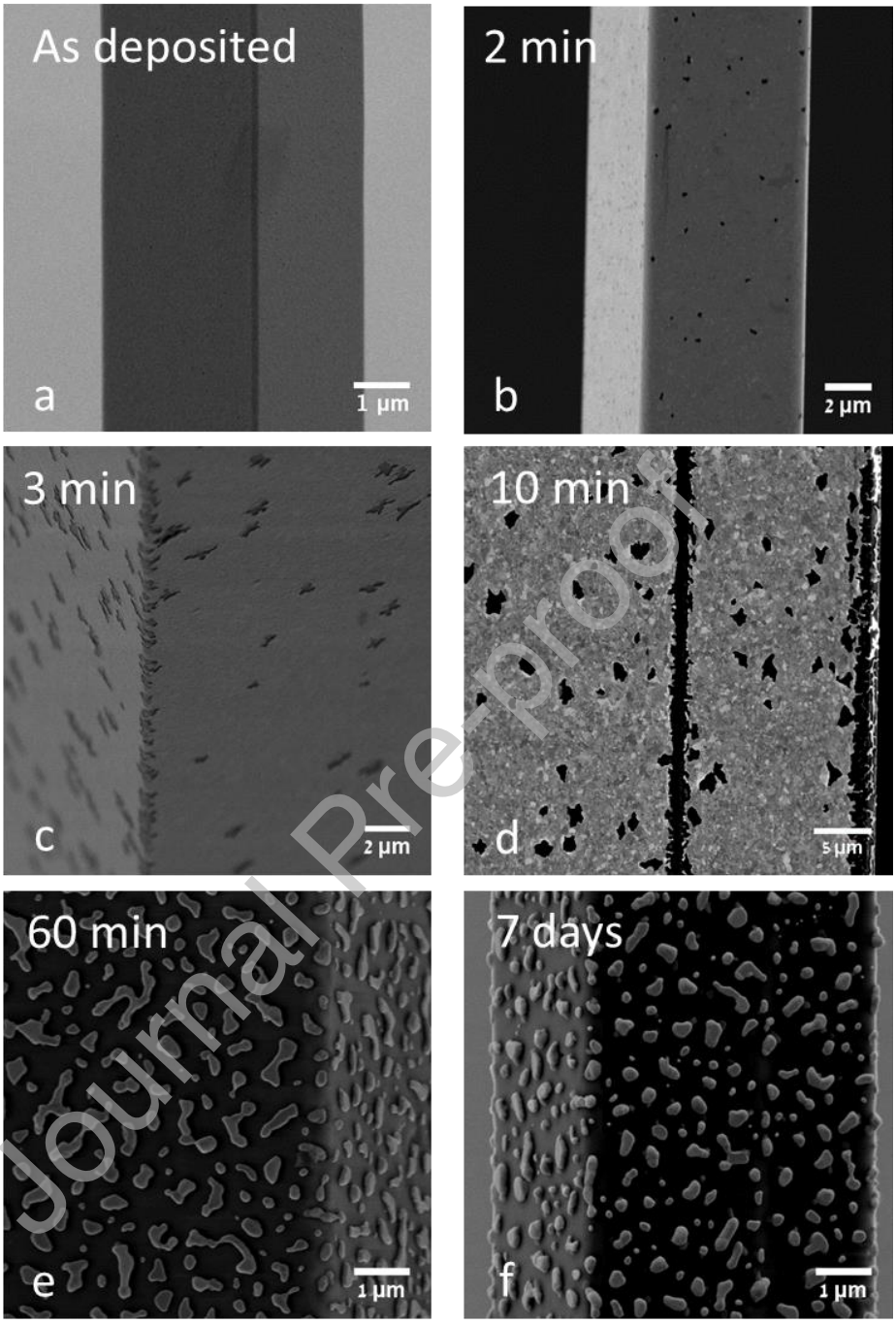

Fig. 5- SEM micrographs of five different Au-coated KCl whiskers in the as-deposited state (a), and after annealing at the temperature of 350 ^{o}C for 2 min (b), 3 min (c), 10 min (d), 60 min (e), and 7 days (f). Note that the acquisition tilt angle slightly varies between images.

We calculated the ratio of the relative exposed area of the KCl whisker along the edges, $a = \frac{Exposed\ edge\ area}{Total\ edge\ area}$, and on the flat facets, $A = \frac{Exposed\ facet\ area}{Total\ facet\ area}$. This ratio, $\frac{a}{A}$, was approximately one during the early (2 min) and the late (60 min, 7 days) stages of SSD. In comparison, after annealing for 3 and 10 min, this ratio was close to two, indicating an accelerated SSD rate along the whisker edges. After the SSD process along the edges has been completed, the process continues on the facets until isolated Au particles are formed there, and the degrees of substrate coverage by the Au particles on the whisker facets and along the edges become similar.

Our experimental results on the SSD of thin Au film deposited on single crystalline KCl whisker raise questions about the physical reasons for the accelerated exposure of the whisker edges. In the next section we formulate a model for the SSD of a single crystalline metal film on a prismatic 3-D substrate with rounded edges and flat facets, and undertake simulations; the role of the anisotropy of the KCl-Au interface in facilitating the SSD process along the whisker edges is discussed in Section 5.

4. Modeling – Evolution of holes on a rounded substrate

Inspired by our experimental results we further investigated the evolution of 3D films with holes of various sizes and shapes on a rounded substrate, assuming that the surface topography evolves by the surface diffusion mechanism. By assuming that the holes have two mirror symmetry planes, (one along the whisker edge and another one along the whisker perimeter, in the hoop direction), we need only to consider the behavior of one quarter of the hole.

In our model the whisker's growth direction is parallel to the x-axis, and the side facets are parallel to xy and xz planes, where the xz facet will be the facet examined in the model, see

Fig. 6. In the yz cross section, the substrate appears as a rectangle with rounded edges. The exterior dimensions of the system are limited by a bounding elliptic cylinder. The exterior surface of the film is assumed to evolve according to motion by surface diffusion, and to intersect the curved substrate at a prescribed contact angle θ_c along a curve which represents the contact line. We refer to a curve along which the exterior surface intersects a mirror plane or a bounding elliptic cylinder as a "free boundary", and we refer to the cross-section or base of the bounding elliptic cylinder as the bounding ellipse. We impose holonomic constraints (See section 2 in the Supplementary materials), Neumann boundary conditions, and no mass flux along the free boundary. Along the contact line, the boundary conditions that we impose are given by a holonomic constraint, balance of mechanical forces (Young's law), and no mass flux. We assume that the exterior surface is a 2D regular parametric surface which is embedded in $\mathbb{R}^3$, and may be described as

$$X(\alpha,\beta,t) = \big(x(\alpha,\beta,t),\ y(\alpha,\beta,t),\ z(\alpha,\beta,t)\big), \quad 0 \le \alpha,\beta \le 1\,,\ \ t \in [0, t_{final}]\,, \qquad (1)$$

where α and β are parametric variables, and t is the annealing time. The typical geometry and initial conditions of our model are shown on the cross section of the rounded substrate along the y-z plane portrayed in Fig. 6.

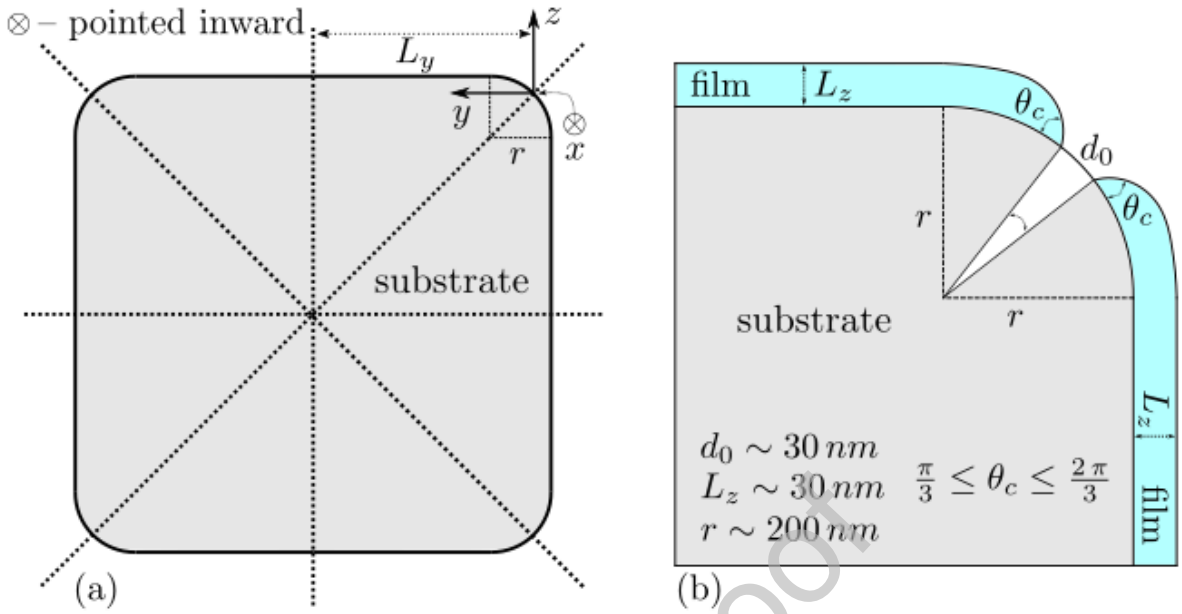

Fig. 6 – A schematic representation describing the typical initial conditions for our numerical simulations of the evolution of holes formed along the substrate edge. The parameters chosen here are roughly in accordance with experiment. L_z is the initial film thickness, r is the radius of the rounded part of the substrate and hence the curvature radius of the substrate edge, and d_0 is the initial diameter of the hole on the substrate.

The parametrization of the various components of the model: mirror planes, bounding elliptical cylinder, substrate and initial conditions are based on previous works [4,36]; details are presented in the Supplementary Materials. Typical parameter values for the model such as film thickness, edge curvature and hole diameter, are indicated in Fig. 6.

4.1. Mathematical formulation

To obtain a dimensionless problem formulation, we rescale all lengths in the system by $\bar{L} = L_z$, where L_z denotes the initial thickness of the solid film far from the contact line, and we rescale time by $\bar{T} = L_z^4/B$, where B is the Mullins' coefficient [37] defined as

$$B = \frac{D_s \nu \Omega^2 \gamma_s}{kT} \ , \tag{2}$$

where D_s, ν, Ω and γ_s are the surface self-diffusion coefficient, the number of mobile atoms per unit area of the surface, the atomic volume, and the surface energy of Au, respectively. The factor kT has its usual thermodynamic meaning.

Additional geometric parameters for the model include r, a_0, b_0, L_x, L_y , where r is the substrate edge radius of curvature (see Fig. 6), a_0 and b_0 are used to parameterize the contact line, and L_x, L_y denote the semi-axes of the bounding elliptical cylinder. These parameters have been normalized by $\bar{L}$. The motion of the exterior film surfaces is governed by the surface diffusion, namely $\langle X_t, \vec{n} \rangle = -\Delta_s H$, where $\langle \cdot, \cdot \rangle$ denote the Euclidean inner product between two vectors in R^3, $\vec{n}$ is the unit normal vector, H is the mean curvature of the surface, and Δ_s is the surface Laplacian [36]. We also impose uniform grid spacing $\|X_\alpha\|_\alpha = 0$; $\|X_\beta\|_\beta = 0$, which helps to improve numerical performance.

4.2. Numerical results

We used the model to investigate the evolution of a hole in a film on a curved substrate. We considered three different contact angles $\theta_c \in \{60°, 90°, 120°\}$ and three (normalized) substrate edge radii of curvature, $\frac{r}{\bar{L}} \in (0.1,1,10)$. In terms of the experiment, we expect that 90°<θ_c<120° and 5< $\frac{r}{\bar{L}}$<50. In accordance with the experimental observations, the initial hole radius ($a_0 = b_0 = \frac{d_0}{2}$) was chosen to be equal to the film thickness, $\frac{a_0}{\bar{L}} = \frac{b_0}{\bar{L}} = 1$, which also roughly

corresponds to the initial grain size in the Au film (See Fig. 5b). The grain boundary grooving and hole nucleation were not considered in our model.

Fig. 7 shows the time evolution of the semi-axes $x_c(t)$ and $y_c(t)$ of the roughly elliptic holes for different edge curvatures and contact angles. The semi-axes are normalized by their initial values, a_0 and b_0. In all cases the hole expansion along the whisker axis (x-axis) is faster than in the hoop direction (y-axis). An abrupt acceleration of axial hole expansion is observed for small radii of curvature (Fig. 7a, b and d, and Supplementary Movie 1). The physical reason for this acceleration is an interplay between hole growth along the edge by surface diffusion and the decrease in film thickness along the edge outward in the hoop directions. For small radii of curvature the latter leads to a rapid decrease of the local film thickness along the edge, which in turn accelerates the axial expansion rate of the hole (which scales as $1/L_z^3$ in planar geometries [1,38]). Acceleration of the axial hole expansion is less pronounced for larger radii of curvature (see Fig. 7c and d, and Supplementary Movie 2) which are more in accord with our experimental conditions; however even in this case the hole can develop anisotropy of up to a factor of two in the axial direction.

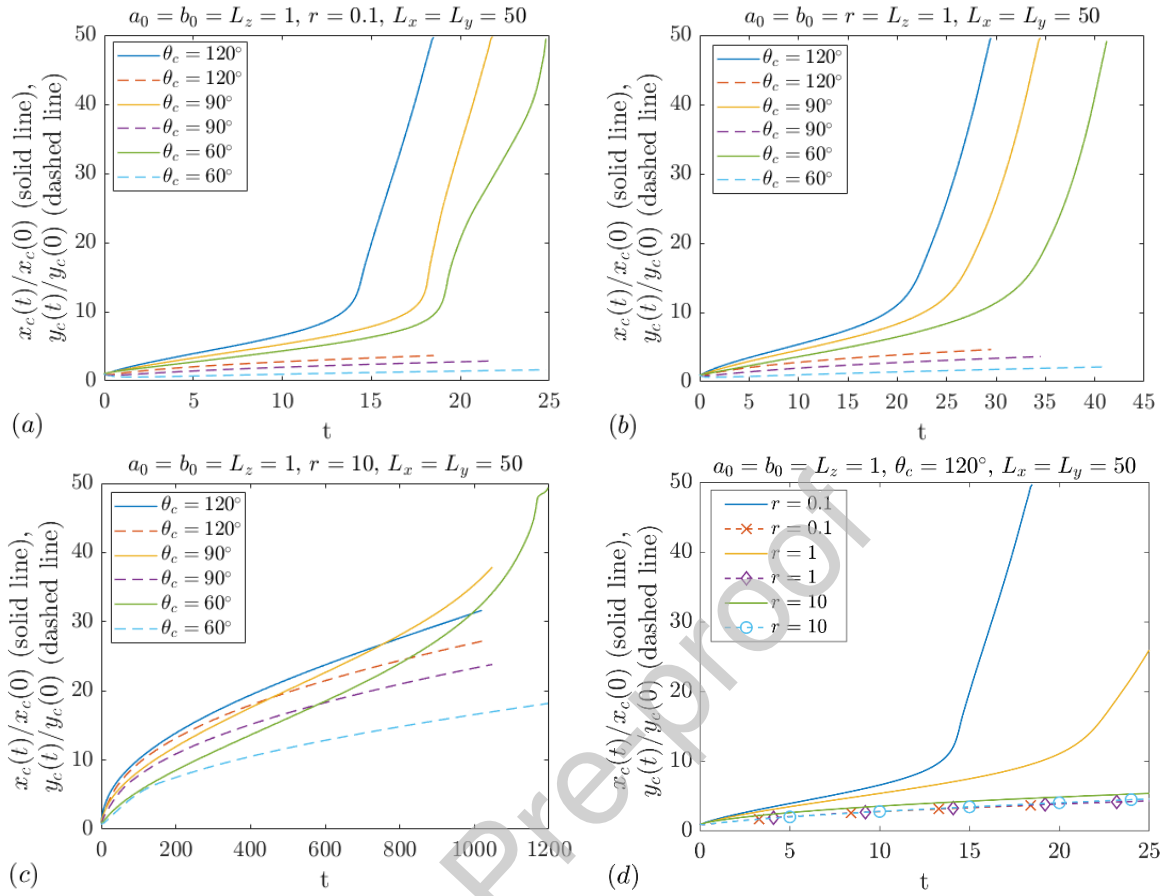

Fig. 7 – The evolution of the normalized semi-axes, $x_c(t)/x_c(0)$ (solid line), $y_c(t)/y_c(0)$ (dashed line), for $\theta_c \in (60°, 90°, 120°)$, and for radius of curvature of the substrate edge, $r/\bar{L}$, of (a) 0.1, (b) 1 and (c) 10. In (d) we compare the evolution of the normalized semi-axes for times $t \in [0,25]$, contact angle $\theta_c = 120°$, and $r/\bar{L} \in (0.1, 1, 10)$. Note the difference in time scales: (a) and (d) $t \in [0,25]$, (b) $t \in [0,45]$, and (c) $t \in [0,1200]$. The initial evolution of $x_c(t)/x_c(0)$ and $y_c(t)/y_c(0)$ of (a)-(c) for $t \in [0,0.5]$ is shown in Fig. S3 of the Supplementary Material. Similarly, the initial evolution of $x_c(t)/x_c(0)$ and $y_c(t)/y_c(0)$ of (b) and (c) for $t \in [0,25]$ is shown in Fig. S4 of the Supplementary Material.

The results indicate that increasing the contact angle, θ_C, when $r/\bar{L} = 0.1$ and 1 accelerates the SSD process in both directions (Fig. 7a, b). This is understandable, since the rim curvature driving the surface diffusion increases with increasing θ_c. However, for the high curvature radius of the substrate edge, $r/\bar{L} = 10$, the dewetting is initially faster for higher contact angle but then

the trend changes and the hole expands faster for lower angles. For $\theta_C = 120°$ and $r/\bar{L} = 10$ (green curves, Fig. 7c) an abrupt acceleration of the hole expansion was not observed during the time span of the simulations, and the hole remained nearly circular. This anomaly can be attributed to the interference of the hole boundary conditions with the imposed boundary conditions along the bounding elliptical cylinder; namely holonomic constraints and mass conservation. In fact, a slow-down is observed in all cases for this reason, as can be seen in Fig. 7a for $\theta_C = 60^o$.

We observed another interesting trend when we carefully examined the initial stage of the hole evolution (see Figs S3-S4 in the Supplementary Information). For all three edge curvatures, the hole initially contracts and only afterwards begins to grow, with expansion in the axial direction (x-axis) starting much earlier than in the hoop direction. The model also predicted complete annihilation of the hole when its initial diameter was smaller than roughly half the film thickness (see Supplementary Movie 3). This observation is in good agreement with the early analysis of Srolovitz and Safran [38], as well as the more recent numerical analysis of Derkach *et al.* [39]. This phenomenon of hole annihilation is related to the 3D nature of the mean surface curvature at the hole edge. Indeed, when the hole radius is small, the negative radial curvature of the surface at the hole edge is higher than positive surface curvature in the mirror plane, thus promoting the surface diffusion from the flat facets to the hole and causing the hole contraction. The initial hole diameter for the simulations shown in Fig. 7 is only twice the critical value for hole annihilation, thus initially the net driving force for the hole expansion is relatively low and some transient hole contraction can occur.

The differences in the time scales seen in Fig. 7 emphasize the significance of the effect of edge curvature on the dewetting kinetics. The time scale when $r/\bar{L} = 10$ is nearly two orders of

magnitude larger than when $r/\bar{L} = 0.1$. Thus, the dewetting is extremely fast in regions of high edge curvature. This dewetting acceleration by the edge curvature is in qualitative agreement with our experimental observations; however, the typical curvature of the whisker edge in the experiment is somewhat smaller than in the simulations. Moreover, the SSD behavior of the thin Au coating on the KCl whiskers observed in the experiment is affected by a number of factors which cannot be accounted for by a model based solely on surface diffusion, such as the grain boundary grooving, thermal stresses, and the varying nature of the Au-KCl interface at the whisker edge. These physical factors are discussed below.

5. Discussion

5.1. The role of thermal stresses

Elastic stresses in the film can change the driving force for the SSD and thus affect its kinetics [40]. This is because hole formation in the film relaxes part of the elastic strain energy, thus increasing the driving force for dewetting. The elastic stresses in the film arise because of thermal expansion mismatch between the film and the substrate, as formulated by Stoney [41]. In the case of large patches of a thin film deposited on a flat substrate, the stress concentration along the edges is negligible. In this case the biaxial stress in the film can accelerate the dewetting, but cannot lead to anisotropic hole growth.

In our case of the core-shell structure formed by the KCl whiskers and Au coating, the KCl core is allegedly constrained by the gold film surrounding it. In addition, the thermal expansion coefficient of KCl, α_{KCl}, is more than twice as high as the respective coefficient of Au,

α_{Au}, which means that tensile stresses develop in the Au film upon heating to the dewetting temperature of 350 °C. The cross-sectional diameter of the KCl is by about two orders of magnitude larger than the thickness of Au film, so that the thermal expansion of the system is dominated by the whisker. Rough estimation of the thermal stress can be performed by assuming that the KCl expands without constraints, so that all the thermal expansion mismatch strain is absorbed by the Au film. The corresponding thermal strain, ϵ_{th}, is then $\epsilon_{th} = (\alpha_{\mathrm{KCl}} - \alpha_{\mathrm{Au}})\Delta T \approx 7.6 \cdot 10^{-3}$, where ΔT is the difference between the temperature of the SSD and the room temperature. The corresponding stress in the Au film is $\sigma_{Au} = Y\epsilon_{th} \approx 1\ \mathrm{GPa}$, where Y is the biaxial Young's modulus of the film. The prismatic geometry of the Au film relevant for the present study leads to thermal stress concentration along the edges. This stress concentration may cause the accelerated SSD at the whisker edges in two ways:

(i) Fracture of the film at the edges and enhanced hole nucleation just after reaching the dewetting temperature.

(ii) Accelerated hole growth in the axial direction due to the anisotropy of the driving force for dewetting. This is because the elastic stresses in the film contribute to the driving force of dewetting and accelerate its rate [40].

The homogeneous nucleation of the holes observed after the shortest annealing time of 2 min (see Fig. 5b) invalidates the first option. As for the second option, any elastic stress in the polycrystalline thin film can rapidly relax according to the wedge-like grain boundary diffusion mechanism proposed by Gao *et al.* [42]. In this model, stress relaxation occurs by mass transport from the surface into the grain boundaries, where the wedge of extra material compensates for the tensile strain. A rough estimate of the characteristic relaxation time, τ, is given by (see the Supplementary Information for the derivation):

$$\tau \approx \frac{kTdL_z^2}{\delta D_b Y \Omega}, \quad (3)$$

where d, δ, and D_b are the grain size, the width of the grain boundary, and the self-diffusion coefficient of Au along the grain boundaries, respectively. For our estimates, we employed the following values of parameters: Y=135.3 GPa [43], $\delta D_b = 2.3\times10^{-23}$ m^3/s [44], $\Omega=1.7\times10^{-29}$ m^3, and $d\approx$30 nm. The characteristic thermal stress relaxation time obtained with the aid of Eq. (3) is then 4.4 μs, many orders of magnitude shorter than the shortest time for the SSD treatment performed in this study (2 min). Thus, we can safely conclude that thermal stresses do not play any significant role in preferential exposure of the whisker edges.

5.2. The onset of dewetting at the whisker edges

It has been established in the literature [1] that the rate of SSD (which include both the nucleation of holes and their expansion) scales inversely with the film thickness on flat substrates. Therefore, it appeared very important to verify that the observed acceleration of SSD at the whisker edges is not correlated with the local variation of the film thickness. Indeed, we verified film uniformity in every batch (Fig. 2), and observed only slight variation of the thickness in the range of 20-30 nm between the batches, but neither within a single batch nor at different locations on a single whisker. This means that dewetting rates can vary between samples from different batches, but should be the same for whiskers within the same sample. Moreover, the uniformity of the Au film thickness in the case of individual whiskers indicates that reasons other than the local variation in film thickness should be sought to explain the

preferential exposure of the whisker edges. According to the model formulated in Section 4, the edge curvature imposed by the whisker on the Au film may accelerate the expansion of dewetting holes in the axial direction.

5.3. Curvature-driven hole growth by surface diffusion

The kinetics of hole growth is controlled by self-diffusion of Au atoms on the surface driven by the gradient of the surface chemical potential, which scales with the mean surface curvature H, as described in Section 4. The initial curvature of the Au film at the edges of the KCl whisker leads to the surface diffusion controlled out-diffusion of Au atoms to the flat facets and concomitant decrease of the local film thickness along the edges. In terms of the expanding dewetting holes this implies higher local dewetting front velocity in the axial direction, as reproduced in our numerical model (see Section 4). Our model indicated the onset of hole acceleration in the axial direction at some critical time; we conjecture that this reflects critical thinning of the film along the edge (see Fig 7a, b). In the experimental system, the anisotropic growth results in elliptically-shaped holes with the aspect ratio increasing with time until two neighboring holes merge, or an isolated island is formed. This anisotropic hole growth results in the merging of holes along the axial direction at the early stages of the SSD, leading to early exposure of the KCl whisker edges. However, our numerical results demonstrate that the acceleration of dewetting holes growth in the axial direction crucially depends on the ratio of the edge radius of curvature to the initial film thickness, $r/\bar{L}$. In our experiments we observed the preferential exposure along the whisker edges during hole growth in all cases studied, irrespective of the edge curvature. This appears to indicate that while the mechanisms considered in Section 4 are certainly at play, additional factors causing accelerated SSD along the whisker

edges should be considered. As pointed out in Section 5.1, these mechanisms cannot be associated with variations in the hole nucleation rate which depends on the location on the whisker, since homogeneous distribution of holes was observed after the shortest annealing time of 2 min (see Fig. 5b). Thus, apparently the holes nucleate at random defects in the Au film which are homogeneously distributed within the film. Therefore, the early exposure of the whisker edges should be associated with the anisotropic axial growth of the dewetting holes located along the edges.

It is reasonable to assume that an important factor contributing to the anisotropic growth of the edge holes is associated with the anisotropic energy of the Au-KCl interface. Typically, the curvature of the hole rim increases with increasing contact angle, θ_c, which is determined by the Young equation:

$$\cos\theta_c = \frac{\gamma_{\text{sub}} - \gamma_{\text{int}}}{\gamma_s}\ , \qquad (4)$$

where γ_{sub} and γ_{int} are the surface energy of the KCl substrate and the energy of the Au-KCl interface, respectively. In Eq. (4), the angular anisotropy of the surface energy of Au (Herring's torque) has been neglected. While the relative variations of the surface energy of inorganic crystals with different surface orientations rarely exceed 2-3%, the energies of the solid-solid interface vary within much wider limits, depending on the degree of atomic matching at the interface [45]. The texture of the Au films deposited on the flat KCl (100) wafer shows two preferred ORs with two additional twinning-related variants (see Figs 3 and 4). This indicates that the observed ORs correspond to the local minima of γ_{int} with respect to interface orientation. Fecht and Gleiter suggested a lock-in rows model to describe the dependence of the interphase

boundary energy on the orientation relationship between the two phases and the lattice parameter mismatch [46]. In the lock-in configuration the densely packed rows of atoms in the noble metal film match into the valleys between the surface atoms of the ionic crystal. The lowest energy lock-in configuration is achieved for a specific orientation, which allows the highest number of coincidence sites between the metal atom rows and the ionic crystal valleys. Generally, the ORs between the Au grains and KCl crystal determined in the present study are consistent with the lock-in model of Fecht and Gleiter, which means that they correspond to the interfaces of low energy. The orientation varies along the KCl whisker edge from a (100) facet to the normal (010) facet. The gradual change in orientation makes the out of-plane orientation of the substrate relative to the film different from that of the flat facets. The change in orientation results in a decrease in the degree of atomic matching at the interface, with concomitant increase in the energy of the Au-KCl interface, γ_{int}. According to Eq. (4), an increase in γ_{int} causes an increase in the contact angle θ_c, and subsequently leads to an increase of the local surface curvature at the hole rim and an increase in the local dewetting front migration rate. When an initially circular hole nucleates along the whisker edge, it firstly expands isotropically in all directions. However, hole expansion in the hoop direction soon results in arrival of a dewetting front at the flat {100} facets, with corresponding low values of γ_{int} and θ_c, resulting in slowdown of the hoop expansion rate. However, the expansion rate in the axial direction remains consistently high, resulting in anisotropic holes which are elongated in the axial direction, and in early exposure of the whisker edges. The proposed mechanism of accelerated edge dewetting does not depend strongly on the curvature of the whisker edges. It should be noted that the mechanism outlined above, and the curvature-related mechanism considered in Section 4 are additive, with the latter mechanism taking a lead for the whiskers with sharp edges, and at the late stages of edge holes growth.

6. Summary

From the results of the present study, the following conclusions can be drawn:

1. We synthesized hierarchical core-shell Au-KCl whiskers consisting of a single crystalline, [001]-oriented rectangular KCl core of 0.05-5 mm in height and 0.5-20 μm in diameter, with a conformal nanocrystalline Au shell of 20-30 nm in thickness. The radius of curvature along the whisker edges varied from few hundreds of nanometers to 1-2 μm.

2. Isothermal annealing of the core-shell whiskers at the temperature of 350 °C resulted in accelerated solid state dewetting of the Au shell along the whisker edges and in early exposure of the KCl edges. Moreover, the nucleation rate of the dewetting holes was homogeneous, with no preference to any specific location on the whisker.

3. Inspired by our experimental observations of enhanced SSD along the whisker edges, we formulated a mathematical model for dewetting hole growth along the curved whisker edges. The model which was based on curvature-driven surface self-diffusion, predicts anisotropic hole growth along the whisker edges, with the axial (along the whisker axis) hole growth rates being significantly higher than the growth rates in the hoop direction. Numerical results (see Fig. 7 in the text as well as Figs S3-S4 and Movies 1-3 in the Supplementary Materials) indicated that the aspect ratio of the holes along the edges strongly depends on the curvature radius of the substrate edge, with smaller radii of curvature resulting in higher anisotropies.

4. We demonstrated that the thermal stresses developing in the Au shell due to the mismatch of thermal expansion coefficients of Au and KCl are short-lived and cannot explain the observed SSD behavior of the Au film.

5. The preferential ORs of the Au grains on the flat (001) KCl substrate were found to be $(111)_{Au}\|(001)_{KCl}$, $[1\bar{1}0]_{Au}\|[010]_{KCl}$ and $[\bar{1}\bar{1}2]_{Au}\|[001]_{KCl}$. We identified these ORs with the energy

minima of the Au-KCl interface, as is consistent with the lock-in rows model of Fecht and Gleiter. We then related the higher growth rates of the holes along the edges of the KCl whiskers with the higher energy of the interfaces between the Au film and the KCl crystal with the orientations intermediate between those of (100) and (010).

Finally, the results of this work demonstrate that the SSD of thin metal films deposited on curved substrates can be understood in terms of an interplay between the curvature-driven surface diffusion and the driving force for dewetting which depends on crystallographic degrees of freedom of the interface.

Declaration of interests

☒ The authors declare that they have no known competing financial interests or personal relationships that could have appeared to influence the work reported in this paper.

Acknowledgements

This work was supported by the US-Israel Bi-National Science Foundation (BSF), grant No 2014398 (EA, AS, JRG, and ER) and by the Israel Science Foundation (ISF), grant No. 1200/16 (VD and AN-C). Helpful discussions with Dr. Leonid Klinger and Dr. Nimrod Gazit are heartily acknowledged.

References

[1] C. V. Thompson, Solid-State Dewetting of Thin Films, Annu. Rev. Mater. Res. 42 (2012)

399–434. doi:10.1146/annurev-matsci-070511-155048.

[2] C. V Thompson, Grain Growth in Thin Films, Annu. Rev. Mater. Sci. 20 (1990) 245–268. doi:10.1146/annurev.ms.20.080190.001333.

[3] E. Rabkin, D. Amram, E. Alster, Solid state dewetting and stress relaxation in a thin single crystalline Ni film on sapphire, Acta Mater. 74 (2014) 30–38. doi:10.1016/j.actamat.2014.04.020.

[4] V. Derkach, A. Novick-Cohen, A. Vilenkin, E. Rabkin, Grain boundary migration and grooving in thin 3-D systems, Acta Mater. 65 (2014) 194–206. doi:10.1016/j.actamat.2013.10.061.

[5] D.J. Srolovitz, On the stability of surfaces of stressed solids, Acta Metall. 37 (1989) 621–625.

[6] D.M. Mattox, Thin film metallization of oxides in microelectronics, Thin Solid Films. 18 (1973) 173–186. doi:10.1016/0040-6090(73)90096-5.

[7] W.M. Abbott, S. Corbett, G. Cunningham, A. Petford-Long, S. Zhang, J.F. Donegan, D. McCloskey, Solid state dewetting of thin plasmonic films under focused cw-laser irradiation, Acta Mater. 145 (2018) 210–219. doi:10.1016/J.ACTAMAT.2017.12.030.

[8] D. Wang, P. Schaaf, Plasmonic nanosponges, Adv. Phys. X. 3 (2018) 1456361. doi:10.1080/23746149.2018.1456361.

[9] J. Mizsei, Activating technology of SnO_2 layers by metal particles from ultrathin metal films, Sensors Actuators B Chem. 16 (1993) 328–333. doi:10.1016/0925-4005(93)85204-N.

[10] L. Armelao, D. Barreca, G. Bottaro, A. Gasparotto, S. Gross, C. Maragno, E. Tondello, Recent trends on nanocomposites based on Cu, Ag and Au clusters: A closer look, Coord.

Chem. Rev. 250 (2006) 1294–1314. doi:10.1016/j.ccr.2005.12.003.

[11] S.J. Randolph, J.D. Fowlkes, A. V. Melechko, K.L. Klein, H.M. Meyer, M.L. Simpson, P.D. Rack, Controlling thin film structure for the dewetting of catalyst nanoparticle arrays for subsequent carbon nanofiber growth, Nanotechnology. 18 (2007) 465304. doi:10.1088/0957-4484/18/46/465304.

[12] V. Schmidt, J. V. Wittemann, S. Senz, U. Gösele, Silicon nanowires: A review on aspects of their growth and their electrical properties, Adv. Mater. 21 (2009) 2681–2702. doi:10.1002/adma.200803754.

[13] D. Tsivion, M. Schvartzman, R. Popovitz-Biro, E. Joselevich, Guided Growth of Horizontal ZnO Nanowires with Controlled Orientations on Flat and Faceted Sapphire Surfaces, ACS Nano. 6 (2012) 6433–6445. doi:10.1021/nn3020695.

[14] L.R. Meza, S. Das, J.R. Greer, Strong, lightweight, and recoverable three-dimensional ceramic nanolattices., Science. 345 (2014) 1322–6. doi:10.1126/science.1255908.

[15] M. Mieszala, M. Hasegawa, G. Guillonneau, J. Bauer, R. Raghavan, C. Frantz, O. Kraft, S. Mischler, J. Michler, L. Philippe, Micromechanics of Amorphous Metal/Polymer Hybrid Structures with 3D Cellular Architectures: Size Effects, Buckling Behavior, and Energy Absorption Capability, Small. 13 (2017) 1602514. doi:10.1002/smll.201602514.

[16] Fin FET devices from bulk semiconductor and method for forming, (2002). https://patents.google.com/patent/US6642090B1/en (accessed May 2, 2019).

[17] X. Xia, C. V. Di Leo, X.W. Gu, J.R. Greer, In Situ Lithiation-Delithiation of Mechanically Robust Cu-Si Core-Shell Nanolattices in a Scanning Electron Microscope, ACS Energy Lett. 1 (2016) 492–499. doi:10.1021/acsenergylett.6b00256.

[18] C. Herring, Surface Tension as a Motivation for Sintering, in: Fundam. Contrib. to Contin.

Theory Evol. Phase Interfaces Solids, Springer Berlin Heidelberg, Berlin, Heidelberg, 1999: pp. 33–69. doi:10.1007/978-3-642-59938-5_2.

[19] A.L. Giermann, C. V. Thompson, Solid-state dewetting for ordered arrays of crystallographically oriented metal particles, Appl. Phys. Lett. 86 (2005) 1–3. doi:10.1063/1.1885180.

[20] L. Klinger, E. Rabkin, Capillary-driven motion of nanoparticles attached to curved rigid substrates, Acta Mater. 60 (2012) 6065–6075. doi:10.1016/j.actamat.2012.07.043.

[21] W. Jiang, Y. Wang, D.J. Srolovitz, W. Bao, Solid-state dewetting on curved substrates, Phys. Rev. Mater. 2 (2018) 113401. doi:10.1103/PhysRevMaterials.2.113401.

[22] R.W. Balluffi, S.M. Allen, W.C. Carter, Kinetics of Materials, John Wiley & Sons, Hoboken, 2005. doi:10.1002/0471749311.

[23] V. Derkach, A. Novick-Cohen, A. Vilenkin, Grain Boundary Migration with Thermal Grooving Effects: A Numerical Approach, J. Elliptic Parabol. Equations. 2 (2016) 389–413. doi:10.1007/BF03377411.

[24] H. Zhang, Formation of Salt Crystal Whiskers on Nanoporous Coatings and Coating onto Open Celled Foam, Ph.D. Thesis, U. of Minnesota (2012).

[25] H. Zhang, Z. Wu, L.F. Francis, Formation of salt crystal whiskers on porous nanoparticle coatings., Langmuir. 26 (2010) 2847–56. doi:10.1021/la902902k.

[26] Z. Gyulai, Festigkeits- und Plastizitfitseigenschaften von NaCl-Nadelkristallen, Zeitschrift für Phys. 138 (1954) 317–321.

[27] T. Shichiri, The growth mechanism of NaCl whiskers, J. Cryst. Growth. 24–25 (1974) 350–353. doi:10.1016/0022-0248(74)90333-9.

[28] L.A. Giannuzzi, F.A. Stevie, A review of focused ion beam milling techniques for TEM

specimen preparation, Micron 30 (1999) 197–204.

[29] S. Ino, D. Watanabe, S. Ogawa, Epitaxial growth of metals on rocksalt faces cleaved in vacuum. I, J. Phys. Soc. Jpn 19 (1964) 881-891.

[30] L. Brück, Die Struktur dünner auf Steinsalz aufgedampfter Metallschichten, Ann. Phys. 5 (1936) 233–257.

[31] D.W. Pashley, The Study Of Epitaxy In Thin Surface Films, Adv. Phys. 5 (1956) 173–240. doi:10.1080/00018735600101175.

[32] D.W. Pashley, M.J. Stowell, M.H. Jacobs, T.J. Law, The growth and structure of gold and silver deposits formed by evaporation inside an electron microscope, Philos. Mag. 10 (1964) 127–158. doi:10.1080/14786436408224212.

[33] D. Amram, E. Rabkin, On the role of Fe in the growth of single crystalline heteroepitaxial Au thin films on sapphire, Acta Mater. 61 (2013) 4113–4126. doi:10.1016/j.actamat.2013.03.038.

[34] C.M. Müller, R. Spolenak, Determination of the Au/SiN_x interfacial energy by AFM and FIB tomography, Surf. Sci. 617 (2013) 94–105. doi:10.1016/j.susc.2013.07.001.

[35] O. Kovalenko, E. Rabkin, Mechano-stimulated equilibration of gold nanoparticles on sapphire, Scr. Mater. 107 (2015) 149–152. doi:10.1016/j.scriptamat.2015.06.007.

[36] V. Derkach, PhD Thesis - Surface and grain boundary evolution in thin single- and poly-crystalline films, Technion IIT, 2016.

[37] W.W. Mullins, Theory of Thermal Grooving, J. Appl. Phys. 28 (1957) 333–339. doi:10.1063/1.1722742.

[38] D.J. Srolovitz, S.A. Safran, Capillary instabilities in thin films. II. Kinetics, J. Appl. Phys. 60 (1986) 255–260. doi:10.1063/1.337691.

[39] V. Derkach, A. Novick-Cohen, E. Rabkin, Grain boundaries effects on hole morphology and growth during solid state dewetting of thin films, Scr. Mater. 134 (2017) 115–118. doi:10.1016/j.scriptamat.2017.02.046.

[40] F. Cheynis, E. Bussmann, F. Leroy, T. Passanante, P. Müller, Stress effects on solid-state dewetting of nano-thin films, Int. J. Nanotechnol. 9 (2012) 396–411. doi:10.1504/IJNT.2012.045344.

[41] G.G. Stoney, The Tension of Metallic Films Deposited by Electrolysis, Proc. R. Soc. A Math. Phys. Eng. Sci. 82 (1909) 172–175. doi:10.1098/rspa.1909.0021.

[42] H. Gao, L. Zhang, W.D. Nix, C. V. Thompson, E. Arzt, Crack-like grain-boundary diffusion wedges in thin metal films, Acta Mater. 47 (1999) 2865–2878. doi:10.1016/S1359-6454(99)00178-0.

[43] W.F. Gale, T.C. Totemeier, Smithells Metals Reference Book, 8th ed., Butterworth-Heinemann, 2003. doi:10.5860/choice.42-1588.

[44] D. Gupta, Grain-boundary self-diffusion in Au by Ar sputtering technique, J. Appl. Phys. 44 (1973) 4455–4458. doi:10.1063/1.1661981.

[45] J.W. Martin, R.D. Doherty, B. Cantor, Stability of microstructure in metallic systems, 2nd ed., Cambridge University Press, 1997. doi:10.1017/cbo9780511623134.

[46] H.J. Fecht, H. Gleiter, A lock-in model for the atomic structure of interphase boundaries between metals and ionic crystals, Acta Metall. 33 (1985) 557–562. doi:10.1016/0001-6160(85)90019-7.

Graphical abstract